ACS Catalysis

Research Article

pubs.acs.org/acscatalysis

Morphology Effect of Ir/$La_2O_2CO_3$ Nanorods with Selectively Exposed {110} Facets in Catalytic Steam Reforming of Glycerol

Xiaoya Huang, Chengxiong Dang, Hao Yu,* Hongjuan Wang, and Feng Peng

School of Chemistry and Chemical Engineering, South China University of Technology, Guangzhou 510640, China

Supporting Information

ABSTRACT: Tuning the morphology of nanocatalysts has been regarded as a powerful approach to high-performance heterogeneous catalysts, since the highly active facets might be selectively exposed to reactants. Herein, we report how the shape effect significantly improves the performance of Ir/$La_2O_2CO_3$ catalyst in the steam reforming of glycerol at high temperatures up to 650 °C toward a sustainable hydrogen production. $La_2O_2CO_3$ nanorods (NRs) with different sizes and aspect ratios were synthesized for supporting Ir nanoparticles. Compared with conventional Ir/$La_2O_2CO_3$, the NR catalysts considerably improved the activity, selectivity, and stability, allowing for a stable hydrogen production for 100 h without obvious deactivation. The role of the NRs was rationalized by XRD, XPS, TPR, TPD, and HRTEM analysis. The high performance of the NR catalyst is elucidated by the formation of hexagonal $La_2O_2CO_3$ NRs with selectively exposed {110} facets under reaction conditions, which strongly interact with Ir catalysts, thereby preventing the tiny catalyst particles from sintering at 650 °C. A mechanistic insight is presented to understand the interaction based on the structure of the $La_2O_2CO_3$ supports.

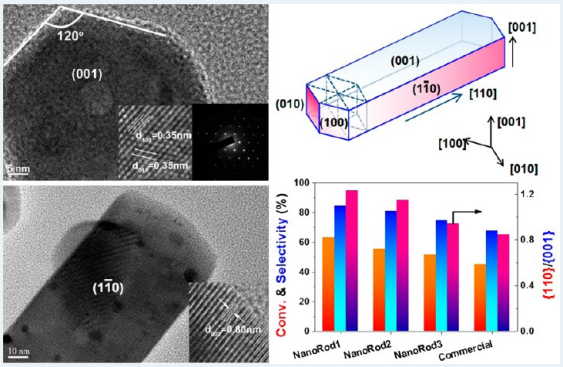

KEYWORDS: *morphology effect, lanthanum dioxycarbonate, metal−support interaction, nanorod, steam reforming of glycerol*

1. INTRODUCTION

The interaction between reactants and specific active sites of solid catalysts plays a central role in heterogeneous catalysis. In principle, engineering the shape of solid catalyst may alter catalytic performances because it creates different types and amounts of active sites, usually located at edges, corners, and high-energy surfaces. This approach to promoting catalyst performances was validated even three decades ago.[1−3] In these early efforts, MoO_3 catalysts with the more {100} planes showed high selectivity toward acrolein from propylene oxidation, whereas {010} planes resulted mainly in deep oxidation to form CO_2.[2]

In this decade, the rapid development of synthesis, properties, and applications of nanomaterials has enabled the controllable preparation of catalytic metals and oxides as nanocatalysts in unprecedentedly delicate morphology.[4−7] Unique shape-dependent catalytic behaviors have been widely reported on these novel catalysts. For instance, tetrahedral Pt nanoparticles (NPs) composed of (111) facets and more sharp edges and corners are more active than cubic ones composed of (100) facets.[8] Tetrahexahedra Pt NPs enclosed by {730} facets exhibit 1.6−4.0 times higher catalytic activity in formic acid electrooxidation compared with conventional spherical Pt NPs.[9] Similar enhancement by exposing high-indexed facets has also been realized for other fcc metals, for example, Pd,[10−12] Au,[13] and Fe.[14] For metal oxides, it has been well-known that TiO_2 with selectively exposed high energy surfaces, for example, {110} and {001}, is much more active for photocatalysis than polycrystalline Degussa P25.[15−17] Rodlike metal oxides show interesting catalysis, represented by the CO oxidation catalyzed by Co_3O_4 nanorods (NRs), on which Co^{3+} in {110} facets acts as active sites.[18] More examples about NR catalysts can be found in the excellent review article from Shen and co-workers.[7] In addition, these oxides with well-controlled shapes can be used as functional supports for metals to improve the metal−support interaction (MSI), for example, CeO_2-supported Au and Pt for water gas shift (WGS), CO oxidation, and amine oxidation.[19−22]

The morphology dependence of nanocatalysts has shown great potential for enhancing catalyst performances; however, its practical application is hindered by a number of issues. One of them is the structural stability of nanomaterials. As the highly energetic surfaces exposed, the increased surface energy of NP system provides the driven force for spontaneously transforming to low energy states, usually spherical particles. So far, nanocatalysts with shape effects have to be used under mild conditions, especially at low to medium temperatures. High temperatures may destroy the sophisticatedly designed structures and deactivate catalysts. In the liquid phase, the more ready dissolution or complexing with ligands at edges,

Received: September 19, 2014
Revised: December 21, 2014
Published: January 9, 2015

DOI: 10.1021/cs5014305
ACS Catal. 2015, 5, 1155−1163

corners, and kinks may induce morphological change of Pt NPs from tetrahedral to spherical shape.[8] Protecting surfactants selectively adsorbed on specific surfaces can effectively maintain NP shapes while hindering the contact between reactants and catalysts.[23] In the gas phase, the reaction temperatures might be extended to 500 °C for WGS on Au/CeO_2 NRs, which benefits from the strong interaction between Au and {111} planes of CeO_2.[19,20] However, to date, the shape effect on the catalysis under harsher conditions has seldom been discussed in publications.[24,25]

The steam reforming (SR) of renewable alcohols, represented by ethanol and glycerol, occurs at medium to high temperatures over supported Ni, Co, Rh, Pt, and Ru catalysts.[26,27] This process produces syngas to enable sustainable hydrogen-based energy technology and fuel manufacture. The thermodynamically optimal temperature has been determined at ∼700 °C.[28,29] It is quite challenging to retain the hydrothermal stability of catalysts at such high temperatures in steam. To overcome this issue, a number of efforts have been devoted to stabilization of metals by strengthening the MSI.[30−34] Herein, we report a new approach to an active and stable catalyst, composed of Ir NPs supported on rod-shaped $La_2O_2CO_3$ as the support.[35,36] The resulting catalyst displayed drastically improved activity and stability for SR reaction of glycerol (SRG) at an unprecedented high temperature: 650 °C. This enhancement can be rationalized by the strong basicity and unique interaction between {110} surfaces of $La_2O_2CO_3$ NRs and Ir NPs.

2. EXPERIMENTAL SECTION

2.1. Synthesis of $La_2O_2CO_3$ NRs. $La_2O_2CO_3$ NRs were synthesized by three methods from the literature to investigate the effect of morphology on catalysis, designated as $La_2O_2CO_3$-r1, $La_2O_2CO_3$-r2, and $La_2O_2CO_3$-r3. For comparison, $La_2O_2CO_3$ without specific shapes was synthesized from commercial La_2O_3 (Sinopharm Chemical Reagent Co., Ltd.), denoted as $La_2O_2CO_3$-c.

Synthesis of $La_2O_2CO_3$-r1. The synthesis is based on a modified version of the precipitation method reported by Li et al.[37] A 200 mL portion of 0.0375 M $La(NO_3)_3$ (Sinopharm Chemical Reagent Co., Ltd.) solution was first mixed with 300 mL of 50 g/L urea aqueous solution in a beaker, then 2 mL of aqueous ammonia was added into the mixture dropwise with agitation. After heating in an oil bath at 90 °C for 3 h, the resulting white suspension was naturally cooled to room temperature. The $La(OH)_3$ precipitate was filtered, washed by DI water and absolute ethanol, and dried at 80 °C. The $La_2O_2CO_3$-r1 sample was obtained by calcination at 500 °C for 2 h.

Synthesis of $La_2O_2CO_3$-r2.[38] In brief, 20 mL of 10% KOH aqueous solution was added into 40 mL 0.0569 M $La(NO_3)_3$ solution dropwise under agitation. After additional agitation for 2 h, the mixture was sealed in a 100 mL autoclave lined with PTEF. After hydrothermal reaction at 180 °C for 12 h, the solid $La(OH)_3$ precipitate was filtered, thoroughly washed by DI water and absolute ethanol, and dried at 80 °C. The $La_2O_2CO_3$-r2 sample was obtained by calcination at 500 °C for 2 h.

Synthesis of $La_2O_2CO_3$-r3.[39] In brief, 1 mL aqueous ammonia was added into 60 mL 0.0736 M $La(NO_3)_3$ solution containing 0.546 g of hexadecyl trimethylammonium bromide (CTAB) as the capping agent under agitation. After additional agitation for 2 h, the mixture was sealed in a 100 mL autoclave lined with PTEF. After hydrothermal reaction at 80 °C for 24 h, the solid $La(OH)_3$ precipitate was filtered, thoroughly washed using DI water and absolute ethanol, and dried at 80 °C. The $La_2O_2CO_3$-r3 sample was obtained by calcination at 500 °C for 2 h.

Synthesis of $La_2O_2CO_3$-c. Commercial La_2O_3 (2 g) was boiled in 200 mL DI water for 2 h. After being filtered and dried at 110 °C, the solids were calcinated at 500 °C for 2 h in CO_2 to convert La_2O_3 to $La_2O_2CO_3$.

2.2. Synthesis of Catalysts. The catalysts were prepared by impregnating appropriate amounts of 3.12 mmol/L $IrCl_3$ solution ($IrCl_3 \cdot nH_2O$; Ir content, 54.51 wt %; Shanghai July Chemical Co., Ltd., China) onto $La_2O_2CO_3$ supports. The impregnated catalysts were dried at 110 °C overnight and then calcined at 500 °C in air for 2 h. The loading of Ir was 3 wt %. See the Supporting Information for more discussion on the preparation conditions.

2.3. Characterizations. Specific surface areas of catalysts were measured by N_2 adsorption at 77 K (ASAP 2010, Micromeritics). Before the measurement, the samples were degassed at 573 K under vacuum overnight. XRD patterns were obtained with a Shimadzu XD-D1 instrument using Cu Kα radiation at 35 kV and 40 mA. The scan rate was 4° min^{-1}. X-ray photoelectron spectroscopy (XPS) was performed with a Kratos Axis ultra spectrometer excited with Al Kα X-ray source. The binding energies (±0.2 eV) were referenced to the C_{1s} peak of adventitious carbon at 284.6 eV. Scanning electron micrographs were obtained in a LEO-1530VP microscope operated at 5 kV. Transmission electron microscopy measurements were performed in an EM-400 or TECNAI10 microscope. Specimens for TEM were prepared by ultrasonically suspending the sample in acetone and depositing a drop of the suspension onto a copper grid covered by amorphous carbon. H_2 temperature-programmed reduction (H_2-TPR) and CO_2 temperature-programmed desorption (CO_2-TPD) were carried out in a TP5080 adsorption instrument equipped with a thermal conductivity detector (TCD) detector. Before H_2-TPR experiments, ∼0.05 g of fresh catalysts were pretreated in N_2 (30 mL/min) at 250 °C for 0.5 h. Then the TPR profile was recorded from 50 to 900 °C at a ramping rate of 10 °C min^{-1} under flowing H_2(10%)/N_2. Before CO_2-TPD experiments, ∼0.1 g samples were pretreated in H_2 (10 v%)/He (30 mL/min) at 500 °C for 0.5 h then were exposed to CO_2 atmosphere at 50 °C for 1 h. After purged with He at 50 °C for an additional 1 h, TPD profiles were recorded from room temperature to 900 °C at a ramping rate of 10 °C min^{-1} under flowing He.

2.4. Catalytic Tests. SRG, oxidative SRG (OSRG), and WGS reactions were performed in a quartz fixed-bed reactor with an inner diameter of 8 mm. The configuration and operation of reactor have been described in our previous work.[35] Before reaction, the catalyst was activated with H_2 at a flow rate of 50 mL/min at 500 °C for 45 min. The gas off the reactor passed through an ice−water cold trap to condense the unreacted glycerol and water. The gaseous products were analyzed by a gas chromatograph equipped with a TCD and a flame ionization detector (FID). A TDX 01 column was used for H_2 analysis in TCD. CO, CH_4, CO_2 and C_2H_4 were analyzed by FID with a packed column for analyzing transformer oil. CO and CO_2 were converted to methane in a methanator packed with Ni catalyst prior to entering the FID.

The glycerol conversion was calculated by

DOI: 10.1021/cs5014305
ACS Catal. 2015, 5, 1155−1163

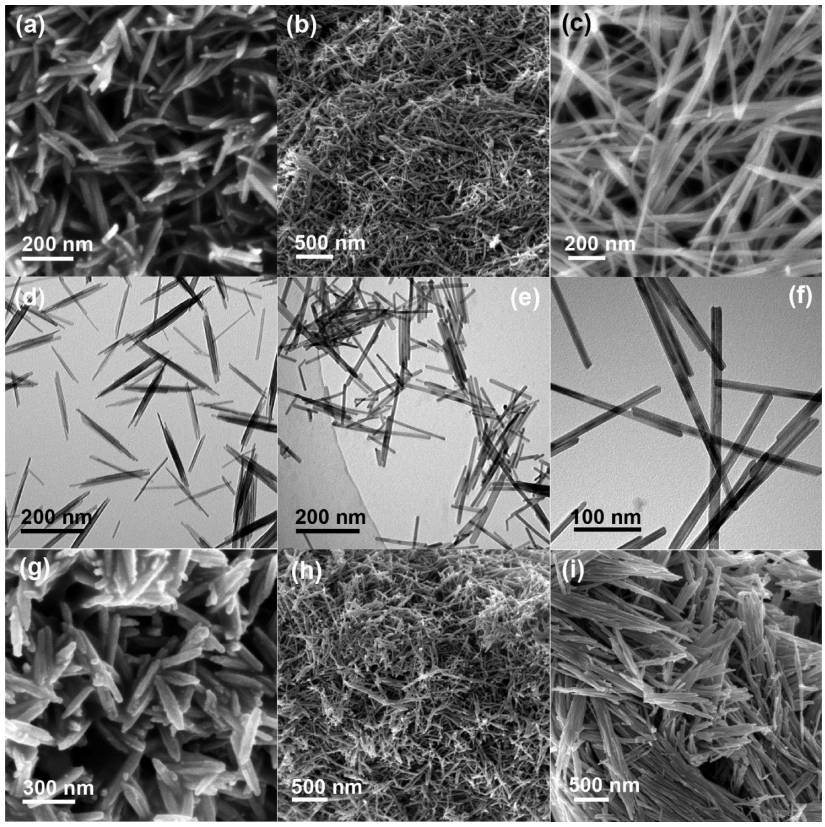

Figure 1. SEM and TEM images of $La(OH)_3$ and $La_2O_2CO_3$ nanorods. (a, d) $La(OH)_3$-r1, (b, e) $La(OH)_3$-r2, (c, f) $La(OH)_3$-r3, (g) $La_2O_2CO_3$-r1, (h) $La_2O_2CO_3$-r2, (i) $La_2O_2CO_3$-r3.

$$X_G = \frac{\text{glycerol}_{\text{inlet}} - 3 \times \text{carbon}_{\text{gas}}}{\text{glycerol}_{\text{inlet}}} \times 100\%$$

where $\text{glycerol}_{\text{inlet}}$ and $\text{carbon}_{\text{gas}}$ represent moles of glycerol fed and carbon detected in th egaseous products.

The selectivity of H_2 was calculated by

$$S_{H_2} = \frac{\text{moles of } H_2 \text{ produced}}{\text{moles of carbon in gas products}} \times \frac{3}{4} \times 100\%$$

The selectivity of the carbon containing species (CO, CO_2, CH_4 and C_2H_4) in the gas products were calculated by

$$S_i = \frac{n \times \text{moles of } i}{\text{moles of carbon in gas products}} \times 100\%$$

where n is the atom number of carbon in i species.

3. RESULTS AND DISCUSSION

3.1. Synthesis of $La_2O_2CO_3$ NRs. As a rare-earth oxide, lanthanum oxide has been widely applied as a catalyst support or promoter. Our previous works have proved that Ir/La_2O_3 catalysts are active and stable for OSR reactions of ethanol and glycerol.[35,36] It was noticed that La_2O_3 transforms to its dioxycarbonate in the presence of steam and CO_2 under reaction conditions through reactions[40,41]

$$La_2O_3 + CO_2 \leftrightarrow La_2O_2CO_3 \quad (1)$$

$$La_2O_2CO_3 + C \rightarrow La_2O_3 + 2CO \quad (2)$$

The strong MSI between Ir and $La_2O_2CO_3$ was responsible for the stability of ethanol reforming at high temperatures up to 650 °C.[36] In this work, we directly synthesized $La_2O_2CO_3$ as the support to reduce the unwanted morphological change during the reaction.

$La_2O_2CO_3$ can be readily formed through calcination of $La(OH)_3$, which is in hexagonal phase (space group: P63/m(176)). We used three methods from the literature to obtain $La(OH)_3$ NRs as precursors of $La_2O_2CO_3$ NRs. Figure 1a–f shows the morphology of $La(OH)_3$ NRs. It can be seen that 1D nanostructures of $La(OH)_3$ were generated either by the precipitation method or by the hydrothermal method described in the Experimental section. An XRD analysis (see Figure S2a in the Supporting Information) shows that these rodlike materials are composed of phase-pure hexagonal $La(OH)_3$ (JCPDS 36-1481). The very thin NRs in $La_2O_2CO_3$-r1 tend to aggregate to form spindle-like bundles.[42] The hydrothermal precipitation assisted by KOH resulted in relatively short and thin NRs of $La_2O_2CO_3$-r2. The introduction of CTAB as a capping agent effectively increased the aspect ratio of $La_2O_2CO_3$-r3, as shown by the dimensional data of these NRs in Table 1. Calcination at 500 °C completely converted

Table 1. Sizes of $La(OH)_3$ Nanorods and Textual Properties of $La_2O_2CO_3$ Nanorods

sample	length, nm	width, nm	aspect ratio	SSA, $m^2\ g^{-1}$	pore volume, $cm^3\ g^{-1}$
$La_2O_2CO_3$-r1	199.8	14.2	14.1	52.7	0.15
$La_2O_2CO_3$-r2	119.3	12.1	9.9	76.0	0.32
$La_2O_2CO_3$-r3	481.2	14.7	32.7	58.9	0.20
$La_2O_2CO_3$-c				5.8	0.05

DOI: 10.1021/cs5014305
ACS Catal. 2015, 5, 1155–1163

Table 2. Catalytic Performances of Ir/$La_2O_2CO_3$ Catalysts in Steam Reforming of Glycerol (SRG), Oxidative SRG (OSRG), and Water Gas Shift (WGS) reactions

	SRG, %[a]					OSRG, %[b]					WGS, %[c]
catalyst	concn	H_2	CO	CH_4	C_2H_4	concn	H_2	CO	CH_4	C_2H_4	concn
Ir/$La_2O_2CO_3$-r1	63.3	84.4	15.8	3.5	3.5	91.9	77.3	23.6	1.8	2.2	82.1
Ir/$La_2O_2CO_3$-r2	55.5	80.9	16.2	4.4	2.7	89.4	69.9	22.2	1.8	2.2	79.8
Ir/$La_2O_2CO_3$-r3	51.6	74.8	24.4	4.9	5.0	90.3	63.8	24.3	2.2	2.3	78.0
Ir/$La_2O_2CO_3$-c	45.3	67.7	28.1	5.5	5.4	83.7	62.7	25.7	2.9	3.1	75.7

[a] T = 650 °C, steam-to-carbon molar ratio = 2, space velocity = 35 $g_{glycerol}$ g_{cat}^{-1} h^{-1}, for 5 h. [b] T = 650 °C, steam-to-carbon molar ratio = 2, carbon-to-oxygen molar ratio = 1, space velocity = 58 $g_{glycerol}$ g_{cat}^{-1} h^{-1}, for 5 h. [c] Steam-to-CO molar ratio = 3, T = 650 °C, gas hourly space velocity = 10 000 h^{-1}, for 5 h. The equilibrium conversion of CO under these conditions is 83.1%, according to $K_p = \exp(4577.8/T - 4.33)$.[43]

$La(OH)_3$ into (hexagonal/monoclinic) $La_2O_2CO_3$ for $La_2O_2CO_3$-r1, -r3, and -c, as shown by XRD patterns in Figure S2b. Only on $La_2O_2CO_3$-r1 was pure hexagonal phase $La_2O_2CO_3$ obtained. Meanwhile, SEM observations indicated that the rodlike morphology was well maintained, as shown in Figure 1g–i. Because of aggregation among NRs, accurately sizing the single NR is difficult; however, the textural measurement displayed the specific surface area (SSA) of $La_2O_2CO_3$ NRs from the thinner $La(OH)_3$ NRs was also higher, which may be used as an indicator of sizes of $La_2O_2CO_3$ NRs. In addition, $La_2O_2CO_3$ NRs exhibit much higher SSAs than $La_2O_2CO_3$-c as a result of their 1D nanostructure.

3.2. Catalytic Performances Improved by NRs. The Ir catalysts supported on $La_2O_2CO_3$ NRs were subjected to SRG, OSRG, and WGS reactions to investigate the shape effect of the support on catalysis. Table 2 compares their catalytic performances (see Figures S3–6 for more catalytic results). In SRG, the NR catalysts were much more active than the commercial one, indicated by the higher conversion of glycerol and H_2 selectivity. Introduction of oxygen can couple the strongly endothermic SR reaction and exothermal oxidation to reduce the energetic requirement of the whole reaction and to relieve the deactivation by coking. Our previous work also demonstrates that the oxidative atmosphere facilitates an in situ dispersion mechanism to stabilize catalytic NPs.[36] As shown in Table 2, the higher conversion was realized in OSRG. Meanwhile, the lower selectivity of C_2H_4, a typical precursor of polymerized condensation, implied the better stability against coking. Similarly, the better activity of NR catalysts was reconfirmed. The three NR catalysts used in this work displayed similar glycerol conversion, but quite different H_2 selectivity in OSRG, suggesting different reaction pathways. WGS reaction was separately tested because it is important to contribute H_2 selectivity by extracting H_2 from steam. The WGS activity showed consistent order with the H_2 selectivity in OSRG, indicating that Ir/$La_2O_2CO_3$-r1 was the choice of catalyst for hydrogen production. Summarizing the above results, the catalytic performances are in a decreasing order of Ir/$La_2O_2CO_3$-r1 > Ir/$La_2O_2CO_3$-r2 > Ir/$La_2O_2CO_3$-r3 > Ir/$La_2O_2CO_3$-c.

It is worth pointing out that the NR catalysts synthesized in this work are very active and selective. Lin has summarized H_2 space time yield (STY) of SRG over various catalysts in literatures in his recent review article.[44] Most of the catalysts reported in the literature have H_2 STY values lower than 2×10^3 (mL g_{cat}^{-1} h^{-1}), among which Ir/CeO_2 is one of the most active catalysts. We calculated our H_2 STY values according to the data in Table 2. In the case of SRG, Ir/$La_2O_2CO_3$-r1 provided H_2 STY of 4.5×10^3 (mL g_{cat}^{-1} h^{-1}); in the case of OSRG, the STY value reached unprecedented 10×10^3 (mL g_{cat}^{-1} h^{-1}). This result demonstrated that the catalyst we developed is excellent.

A medium-term stability test was conducted over Ir/$La_2O_2CO_3$-r1, as shown in Figure 2. Although Ir/$La_2O_2CO_3$ has been proved stable in OSR of ethanol at 650 °C,[36] the more difficult C–C bond breakage for glycerol resulted in a rapid deactivation over 8 h, by a 10% decrease of glycerol conversion and 15% decrease in the H_2 selectivity. All the NR catalysts displayed better stability in SRG and OSRG. In particular, when $La_2O_2CO_3$-r1 was used as the support, not only were the highest initial activity and selectivity achieved, but also the stability was drastically improved, allowing for up to 100 h on-stream without obvious deactivation. Meanwhile, even after 100 h on-stream, the H_2 STY value, 4.5×10^3 (mL g_{cat}^{-1} h^{-1}), was still higher than most of the literature results. The improved stability was also observed under the harsher condition at 58 $g_{glycerol}$ g_{cat} h^{-1} space velocity, as shown in Figure S7. We previously reported an enhancement of catalyst stability by doping Ir/La_2O_3 with calcium.[35] The results here show a totally new methodology to achieve the similar stability by reshaping $La_2O_2CO_3$. More importantly, to our knowledge, it is the first effort to utilize a morphology effect to realize a stable catalyst for such a high temperature reaction up to 650 °C, indicating the huge potential of morphology control.

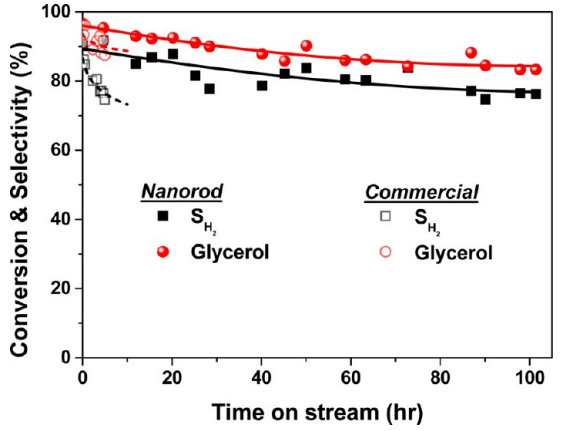

Figure 2. Medium-term stability of Ir/$La_2O_2CO_3$-r1 catalyst in OSRG reaction at space velocity of 29 $g_{glycerol}$ g_{cat}^{-1} h^{-1}. Reaction conditions: steam-to-carbon molar ratio = 2, carbon-to-oxygen molar ratio = 1, T = 650 °C.

3.3. Structure–Activity Relationship. Multiple characterizations were employed to understand the improvement by using NRs and the influencing structural factor of NRs. The physical adsorption measurements, as shown in Table 3, indicate that the NR catalysts have a higher SSA than the

DOI: 10.1021/cs5014305
ACS Catal. 2015, 5, 1155–1163

Table 3. Textual Properties, $La_2O_2CO_3$ Crystalline Sizes and Ir Domain Sizes of Fresh, Reduced and Used Catalysts

	SSA/m^2 g^{-1}			pore volume/cm^3 g^{-1}			$d_{support}$/nm[c]			d_{Ir}/nm[d]
catalyst	fresh	used[a]	used[b]	fresh	used[a]	used[b]	fresh	reduced	used[a]	used[a]
Ir/$La_2O_2CO_3$-r1	27.3	22.5	32.3	0.20	0.23	0.17	18.7	20.4	33.8	3.4
Ir/$La_2O_2CO_3$-r2	35.8	26.9	31.7	0.24	0.15	0.21	14.2	14.4	23.6	3.8
Ir/$La_2O_2CO_3$-r3	25.2	20.7	26.2	0.19	0.19	0.19	17.9	17.1	34.0	2.1
Ir/$La_2O_2CO_3$-c	4.3	3.1	3.8	0.03	0.02	0.03	24.5	21.8	35.1	6.5

[a]OSRG: T = 650 °C, steam-to-carbon molar ratio = 2, carbon-to-oxygen molar ratio = 1, space velocity = 29 $g_{glycerol}$ g_{cat}^{-1} h^{-1}, for 5 h. [b]SRG: T = 650 °C, steam-to-carbon molar ratio = 2, space velocity = 35 $g_{glycerol}$ g_{cat}^{-1} h^{-1}, for 5 h. [c]Calculated by averaging 3 crystallite sizes represented by 3 strong XRD peaks. [d]By TEM statistics.

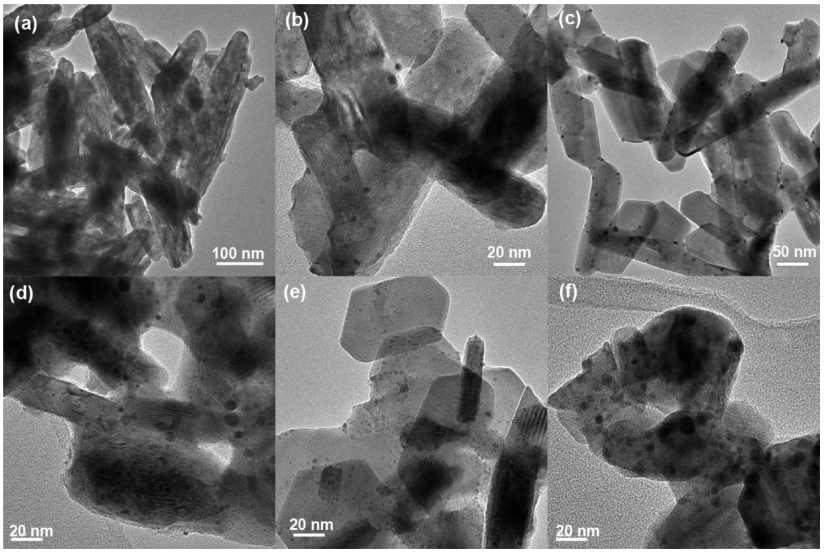

Figure 3. TEM images of (a) reduced Ir/$La_2O_2CO_3$-r1, (b) used Ir/$La_2O_2CO_3$-r1 after 5 h OSRG reaction; (c) used Ir/$La_2O_2CO_3$-r1 after 100 h OSRG reaction; (d–f) used Ir/$La_2O_2CO_3$-r2, Ir/$La_2O_2CO_3$-r3, and Ir/$La_2O_2CO_3$-c, respectively, after 5 h of OSRG reaction. OSRG reaction conditions: steam-to-carbon molar ratio = 2, carbon-to-oxygen molar ratio = 1, T = 650 °C, 29 $g_{glycerol}$ g_{cat} h^{-1}.

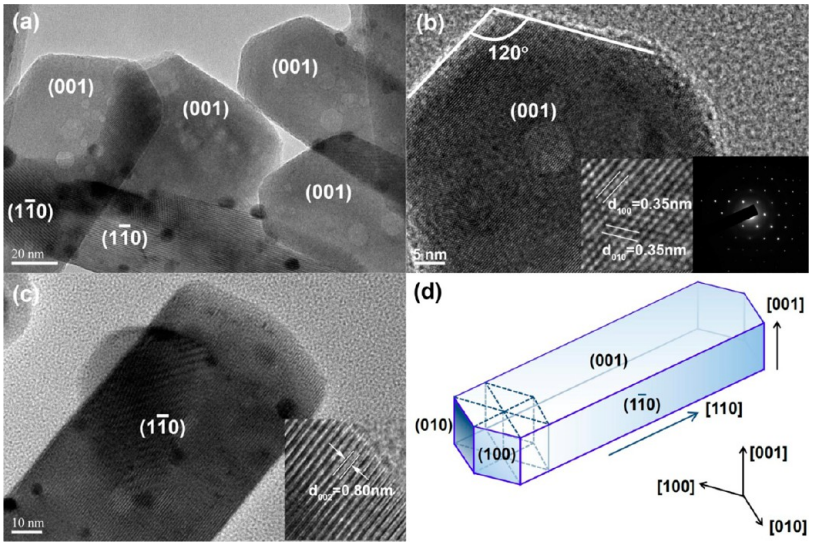

Figure 4. HRTEM (a, b, c) of Ir/$La_2O_2CO_3$−r1 catalyst. The different facets are marked in part a, indicating the preferential exposure of (001) and (1$\bar{1}$0) facets. Parts b and c show the HRTEM images viewed along [001] and [1$\bar{1}$0] directions, respectively. The insets of b and c show the magnified crystalline fringes and electron diffraction pattern. Part d illustrates the shape of $La_2O_2CO_3$ nanorod. OSRG reaction conditions: steam-to-carbon molar ratio = 2, carbon-to-oxygen molar ratio = 1, T = 650 °C, 29 $g_{glycerol}$ g_{cat} h^{-1}, 100 h.

commercial one as a result of the formation of 1D nanostructures. Although the higher SSA may facilitate mass transfer and Ir dispersion, it is unlikely to be the exclusive reason for the improvement. It has been determined that the sizes of Ir NPs can be very small (~2.4 nm after 8 h OSRG; see Table 5 in ref 35) by using La_2O_3 as supports, which can be converted to $La_2O_2CO_3$ during reaction. However, the catalyst suffered from a similar serious deactivation.[35] In addition,

DOI: 10.1021/cs5014305
ACS Catal. 2015, 5, 1155–1163

among the three NR catalysts, the activity cannot be correlated with SSA or Ir dispersion, suggesting other factors dominate.

Ex-situ TEM was used to analyze the structure of working catalysts, represented by used catalysts after OSRG reaction. As shown in Figure 3a, the activation by H_2 resulted in aggregation of NRs to form thicker bundles. Cavities were created on reduced NRs, probably caused by the transformation of $La_2O_2CO_3$ toward $La(OH)_3$ and La_2O_3 due to the generation of water during reduction, as evidenced by XRD patterns in Figure S8. Compared with the irregular particles in $La_2O_2CO_3$-c (Figure 3f), the NR catalysts maintained the 1D structure after OSRG reaction. Especially for $La_2O_2CO_3$-r1, uniform NRs in length of 200−300 nm and width of ∼50 nm were observed even after 100 h of reaction, suggesting the excellent structural stability. On these NRs, Ir NPs were dispersed more homogeneously, as shown in Table 3. Interestingly, a gradual size reduction of Ir NPs from 6.4 to 3.4 and 3.8 nm, from 2−5 and 100 h OSRG reaction, respectively, was observed, indicating the in situ redispersion through MSI.[36] It should be noted that the smaller particle size did not necessarily improve catalysis, indicated by the lower activity of $La_2O_2CO_3$-r3 with the finest Ir domains.

HRTEM analysis allowed us to determine the orientation of NRs. As shown in Figure 4d, a $La_2O_2CO_3$-r1 NR can be viewed as a hexagonal crystallite elongated along the [110] direction. The NR is ended with two obtuse ends in 120° formed by the (010) and (100) surfaces. Around the long axis direction, the NR is enclosed by two (001) flat planes and two $(1\bar{1}0)$ side planes. The similar shape can also be observed with HRSEM. (Figure S9) The orientation is supported by the observation from the [001] and $[1\bar{1}0]$ directions. As shown in Figure 4b, the fringes correspond well to the distances between (100) or (010) planes of hexagonal $La_2O_2CO_3$. The SAED also displays the typical pattern of hexagonal crystallite projected along the [001] direction. The distances between fringes in Figure 4c are consistent with the (002) planes of hexagonal $La_2O_2CO_3$.

Compared with commercial $La_2O_2CO_3$, the elongation in the [110] direction results in the exposure of {110} surfaces in the NR catalysts. Interestingly, the selective residence of Ir NPs on $(1\bar{1}0)$ surfaces, or the equivalent (010) and (100) surfaces, was observed, too. As shown in Figures 3c and 4a, few NPs can be found on (001) surfaces, whereas most of them are enriched on{110} surfaces. This result clearly indicates that the {110} planes play a potent role in the NR-improved catalysis, probably through strong interaction with Ir NPs to stabilize them.

An XRD analysis was used to qualitatively and quantitatively evaluate the anisotropy of NR catalysts. As shown in Figure 5, the intensities of the (100) reflection are very different for the four catalysts used in this work, suggesting different crystallographical orientations of $La_2O_2CO_3$. The intensity ratios, $I_{(110)}/I_{(100)}$ and $I_{(002)}/I_{(110)}$, indicating the aspect ratio and the relative thickness of NRs, respectively, are listed in Table 4. It can be seen that Ir/$La_2O_2CO_3$-r2 has the highest aspect ratio, and Ir/$La_2O_2CO_3$-r3 is the thickest in the [001] direction. However, the lowest $I_{(002)}/I_{(110)}$ for Ir/$La_2O_2CO_3$-r2 and $I_{(110)}/I_{(100)}$ for Ir/$La_2O_2CO_3$-r3 suggest that they are too thin or too short to expose {110} surfaces. To further evaluate the relationship between crystalline orientation and activity, the ratio of {110} to {001} surfaces was estimated as an indicator of the extent of {110} exposure. According to the model in Figure 4d, the approximate area ratio was calculated by

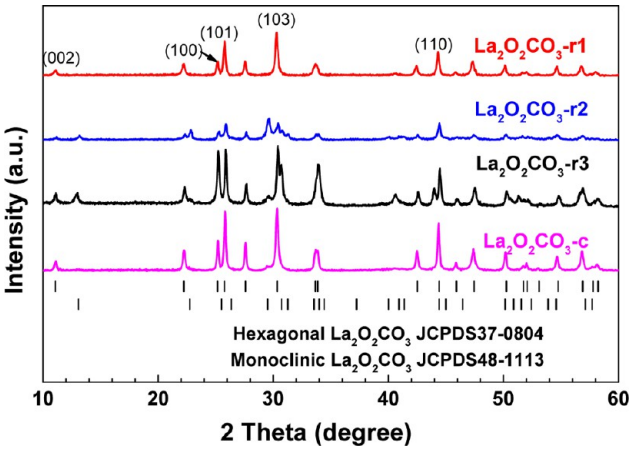

Figure 5. XRD patterns of used Ir/$La_2O_2CO_3$ catalysts after OSRG reaction. Reaction conditions: steam-to-carbon molar ratio = 2, carbon-to-oxygen molar ratio = 1, T = 650 °C, 29 $g_{glycerol}$ g_{cat} h^{-1}, 5 h.

$$\frac{A_{(1\bar{1}0)}}{A_{(001)}} \cong \frac{d_{[001]}}{d_{[1\bar{1}0]}}$$

where d represents crystalline size calculated from specific XRD reflections by Scherrer equation. In this work, $d_{[001]}$ was obtained by averaging d values from the (002) and (004) reflections at 11.15° and 22.30°, respectively, and $d_{[1\bar{1}0]}$ was from the (100) reflection. As shown in Table 4, $A_{(1\bar{1}0)}/A_{(001)}$ values decrease in the order of Ir/$La_2O_2CO_3$-r1 > Ir/$La_2O_2CO_3$-r2 > Ir/$La_2O_2CO_3$-r3 > Ir/$La_2O_2CO_3$-c, being consistent with that of activity displayed in Section 3.2. This result strongly supports that the morphological control of $La_2O_2CO_3$ plays an important role, and the catalytic enhancement is determined by selectively exposed {110} planes.

3.4. Discussion. Hexagonal $La_2O_2CO_3$ is a layered dioxycarbonate, which is stacked by alternate $(La_2O_2)^{2+}$ and CO_3^{2-} layers along the [001] direction. The density functional theory calculation by Wang et al. has shown that the {110} surfaces of $La_2O_2CO_3$ are composed of La and O atoms, and the {001} surfaces contain C and O atoms.[45] Hence, La^{3+}−O^{2-} pairs and the coordinatively unsaturated O^{2-} sites locate on the {110} planes. When {110} planes are selectively exposed, three consequences may be responsible for the shape effects revealed by the aforementioned sections, detailed as follows.

(i) The amounts and types of basic sites depend on the crystallographic orientation of $La_2O_2CO_3$. CO_2-TPD was used to compare the basicity of Ir/$La_2O_2CO_3$ catalysts used in this work. As shown in Figure 6, the three NR catalysts display obviously higher CO_2 desorption due to their increased SSAs. The CO_2-TPD profiles show weak, medium, and strong basic sites in the temperature ranges of 100−170, 180−280, and >280 °C, corresponding to hydroxyl groups, La^{3+}−O^{2-} pairs, and low coordination oxygen anions, respectively.[46] The NR catalysts show intense medium-strength basicity peaks compared with Ir/$La_2O_2CO_3$-c. The highest relative intensity of a medium-strength basicity peak was observed on Ir/$La_2O_2CO_3$-r1, agreeing well with its best catalytic performance. According to Wang et al.,[45] the basic sites contributed by La^{3+}−O^{2-} pairs are mainly located on the {110} surfaces of $La_2O_2CO_3$, which are terminated by La and O atoms. Thus, the basicity results indicate the strong relevance of the forming NR structure exposing {110} surfaces with the improved catalytic performances. The NR catalyst with the higher basicity

DOI: 10.1021/cs5014305
ACS Catal. 2015, 5, 1155−1163

Table 4. Anisotropy of $Ir/La_2O_2CO_3$ Catalysts Revealed by XRD Data in Figure 5

	catalyst			
	$Ir/La_2O_2CO_3$-r1	$Ir/La_2O_2CO_3$-r2	$Ir/La_2O_2CO_3$-r3	$Ir/La_2O_2CO_3$-c
$I_{(110)}/I_{(100)}$	1.69	2.06	0.67	1.59
$I_{(002)}/I_{(110)}$	0.19	0.16	0.30	0.18
$A_{(1\bar{1}0)}/A_{(001)}$	1.23	1.15	0.94	0.85

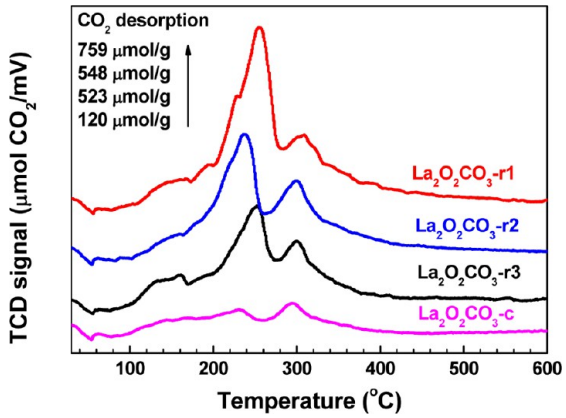

Figure 6. CO_2-TPD profiles of fresh $Ir/La_2O_2CO_3$ catalysts.

is more resistant to coking during SRG and OSRG. In addition, it has been found that the $La^{3+}-O^{2-}$ pairs with medium-strength basicity on $La_2O_2CO_3$ NRs can adsorb and dehydrogenate the alcoholic group of 1-octanol to form alkoxide.[45] Similarly, the −OH group of glycerol or other intermediates of the SRG reaction may be activated on $La^{3+}-O^{2-}$ pairs in {110} surfaces; thereby, the sequential dehydrogenation and C−C bond cleavage may be facilitated on nearby Ir NPs to improve the overall reaction rate of SRG.

(ii) Compared with (001) surfaces, the {110} surfaces of $La_2O_2CO_3$ are more energetic, as revealed by experimental and calculation results.[45,47] Because the selective anchoring on high energy surfaces may reduce the global energy, NPs tend to attach on the {110} surfaces of $La_2O_2CO_3$. This phenomenon has been observed on $Cu/La_2O_2CO_3$ catalysts.[45] As mentioned in Section 3.3, the selective anchoring of Ir NPs was also observed in this work. The contact between NPs and high energy {110} surfaces may lead to a stronger MSI, which can stabilize NPs to prevent sintering at high temperatures. The improved MSI was supported by H_2-TPR and XPS measurements. As shown in Figure 7, the low-temperature reduction peaks at 150−200 °C are attributed to the reduction of iridium oxides, and the peaks at higher temperatures may be caused by the decomposition of $La_2O_2CO_3$ or its transformation to hydroxides.[35,36] It can be clearly seen that the reduction temperature of IrO_2 on NR catalysts is higher than that of a commercial support, indicating the stronger MSI on the {110} surfaces of the NRs. Furthermore, the reduction temperature increases from $La_2O_2CO_3$-r3 to $La_2O_2CO_3$-r2 and $La_2O_2CO_3$-r1, agreeing with the order of {110} exposure and activity, suggesting that the strong MSI is beneficial for catalysis. It was noticed that the low-temperature reduction peak area decreased from $Ir/La_2O_2CO_3$-c, to $Ir/La_2O_2CO_3$-r3, $Ir/La_2O_2CO_3$-r2, and $Ir/La_2O_2CO_3$-r1, resulting in the decreasing apparent oxidation valence of Ir from $IrO_{1.73}$ to $IrO_{1.54}$, $IrO_{1.46}$, and $IrO_{1.24}$, respectively. This might be due to the decomposition of $La_2O_2CO_3$ at medium temperatures, which disturbed the ascription of H_2-TPR profiles because iridium oxides with the stronger interaction with support might by reduced in this temperature range, indicated by the small reduction peak of $Ir/La_2O_2CO_3$-c at 380 °C. Figure 8 shows Ir 4f core−shell XPS

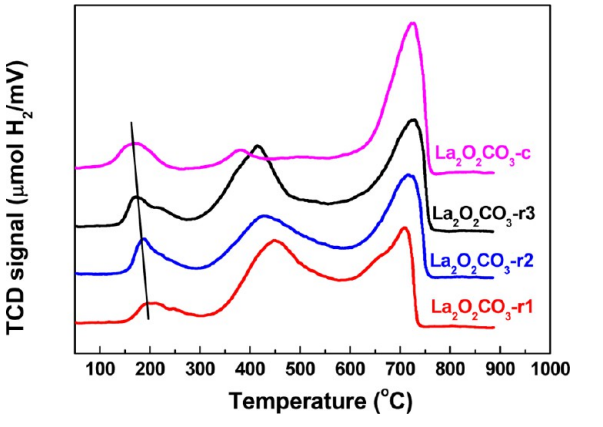

Figure 7. H_2-TPR profiles of fresh $Ir/La_2O_2CO_3$ catalysts.

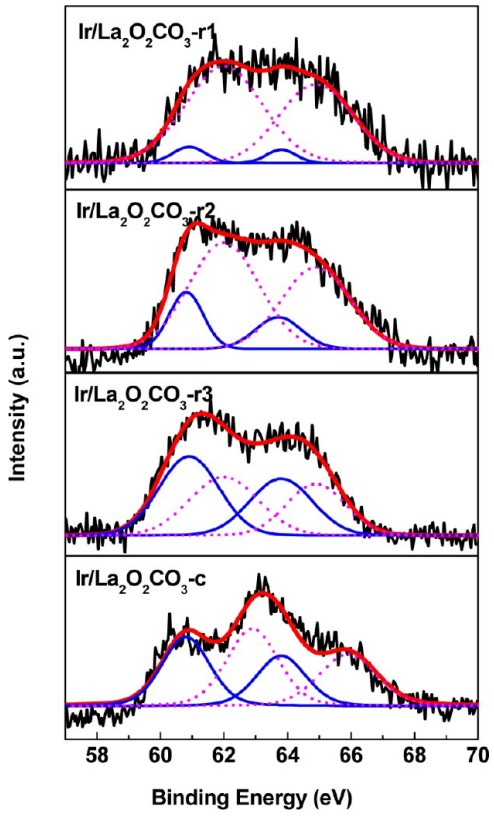

Figure 8. Ir 4f XPS spectra of used $Ir/La_2O_2CO_3$ catalysts. Reaction conditions: steam-to-carbon molar ratio = 2, carbon-to-oxygen molar ratio = 1, T = 650 °C, 29 $g_{glycerol}$ g_{cat} h^{-1}, 5 h. The peaks were deconvoluted with constraints: 2.9 eV of spin-splitting between 4f7/2 and 4f5/2 lines, 4:3 of their area ratio.[48]

DOI: 10.1021/cs5014305
ACS Catal. 2015, 5, 1155−1163

spectra of Ir/$La_2O_2CO_3$ catalysts. Ir 4f doublets split into two sets of peaks at ~60.9 and 62 eV for Ir 4f7/2, representing metallic Ir^0 and $Ir^{\delta+}$ strongly interacted with support, respectively.[35,36] Ir/$La_2O_2CO_3$-r1 has the lowest $Ir^0/Ir^{\delta+}$ ratio of 0.07, indicating that most of the Ir species strongly interact with the support. Being consistent with H_2-TPR results, a quantitative analysis of XPS showed an increasing order of the $Ir^0/Ir^{\delta+}$ ratio (0.07, 0.26, 0.75, 0.84) from Ir/$La_2O_2CO_3$-r1 to Ir/$La_2O_2CO_3$-r2, Ir/$La_2O_2CO_3$-r3, and Ir/$La_2O_2CO_3$-c, demonstrating the gradually decreased MSI. In addition, it should be stressed that the strength of MSI revealed by XPS agrees well with the exposure of {110} surfaces, confirming the structure–activity relationship in Section 3.3.

(iii) The high ratio of the {110} surfaces facilitates the dissolution and exsolution of CO_2 on $La_2O_2CO_3$. A number of works[36,40,41,49] have shown that the formation and decomposition of $La_2O_2CO_3$ are essential to reforming reactions, which can be described by eqs 1 and 2. These reactions allow for gasifying carbon deposited to maintain catalysts stable on stream. In addition, the continuous renewal of catalyst–support interfaces prevents catalysts from sintering, which can be supported by the redispersion of Ir NPs on $La_2O_2CO_3$-r1 from 6.1 nm at 2 h to 3.8 nm at 100 h of OSRG, as mentioned in Section 3.3. Figure 9 illustrates the crystalline structure of

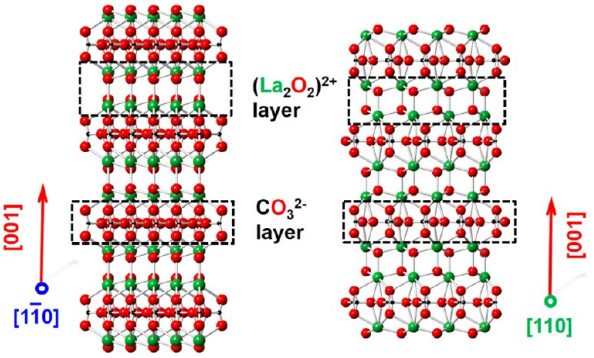

Figure 9. Projections of ball–stick hexagonal $La_2O_2CO_3$ units along the [1$\bar{1}$0] and [110] directions. Green, lanthanum; red, oxygen; black, carbon.

hexagonal $La_2O_2CO_3$ projected along the [1$\bar{1}$0] and [110] directions, exhibiting (1$\bar{1}$0) and (110) surfaces. It is reasonable to infer that eqs 1 and 2 are more likely to occur on the {110} surfaces of $La_2O_2CO_3$ (the side surfaces of Figure 9) because CO_2 can insert or leave solid surfaces from void defects between two $(La_2O_2)^{2+}$ layers via exchanging between O^{2-} and CO_3^{2-}.[50] Although (001) planes may be terminated by carbon and oxygen atoms,[45] the further transformation in bulk is hindered. Hence, the NR catalyst with selectively exposed {110} surfaces displayed better performances, especially a drastically improved stability, as shown in Figure 2. In particular, this mechanism allows for a morphology-dependent catalyst intensification at high temperatures, because eq 1 approaches its equilibrium at ~650–750 °C.[40]

4. CONCLUSIONS

To summarize, $La_2O_2CO_3$ NRs were synthesized by three modified methods from the literature to provide rodlike supports with tunable crystallographic structure. The Ir catalysts supported on NRs showed obvious improvement of activity, selectivity and stability in SRG, OSRG and WGS reactions, demonstrating the effect of morphological control on these high-temperature reactions. The working NR catalysts are enclosed by {110} and {001} surfaces of hexagonal $La_2O_2CO_3$. Ir NPs are selectively anchored on {110} surfaces. The extent of selective exposure of {110} surfaces was found relevant to the catalytic performances. The shape effect of $La_2O_2CO_3$ NR was rationalized by (i) increased medium-strength basic sites on {110} surfaces, which prevent catalysts from coking; (ii) enhanced MSI between Ir NPs and {110} surfaces, which may stabilize Ir NPs to prevent sintering at high temperatures up to 650 °C; and (iii) facile decomposition and regeneration of $La_2O_2CO_3$ via CO_2 insertion from {110} surfaces, which is beneficial for the redispersion of Ir NPs on supports.

■ ASSOCIATED CONTENT

Supporting Information

The following file is available free of charge on the ACS Publications website at DOI: 10.1021/cs5014305.

Nine figures showing experimental results; additional experimental details (PDF)

■ AUTHOR INFORMATION

Corresponding Author

*Phone, Fax: +86 20 8711 4916. E-mail: yuhao@scut.edu.cn.

Notes

The authors declare no competing financial interest.

■ ACKNOWLEDGMENTS

This work was supported by the Natural Science Foundation of China (No. 20176094), Program for New Century Excellent Talents in University (No. NCET-12-0190) and Pearl River Nova Program of Guangzhou City (No. 2011J2200062).

■ REFERENCES

(1) Volta, J. C.; Portefaix, J. L. *Appl. Catal.* **1985**, *18*, 1–32.
(2) Ziółkowski, J. *J. Catal.* **1983**, *80*, 263–273.
(3) Andersson, A.; Hansen, S. *J. Catal.* **1988**, *114*, 332–346.
(4) Zhou, Z.-Y.; Tian, N.; Li, J.-T.; Broadwell, I.; Sun, S.-G. *Chem. Soc. Rev.* **2011**, *40*, 4167–4185.
(5) Zhou, K.; Li, Y. *Angew. Chem.-Int. Ed.* **2012**, *51*, 602–613.
(6) Zaera, F. *ChemSusChem* **2013**, *6*, 1797–1820.
(7) Li, Y.; Shen, W. J. *Chem. Soc. Rev.* **2014**, *43*, 1543–1574.
(8) Narayanan, R.; El-Sayed, M. A. *J. Phys. Chem. B* **2005**, *109*, 12663–12676.
(9) Tian, N.; Zhou, Z. Y.; Sun, S. G.; Ding, Y.; Wang, Z. L. *Science* **2007**, *316*, 732–735.
(10) Tian, N.; Zhou, Z. Y.; Yu, N. F.; Wang, L. Y.; Sun, S. G. *J. Am. Chem. Soc.* **2010**, *132*, 7580–7581.
(11) Yu, Y.; Zhang, Q. B.; Liu, B.; Lee, J. Y. *J. Am. Chem. Soc.* **2010**, *132*, 18258–18265.
(12) Collins, G.; Schmidt, M.; O'Dwyer, C.; McGlacken, G.; Holmes, J. D. *ACS Catal.* **2014**, *4*, 3105–3111.
(13) Liao, H. G.; Jiang, Y. X.; Zhou, Z. Y.; Chen, S. P.; Sun, S. G. *Angew. Chem. -Int. Ed.* **2008**, *47*, 9100–9103.
(14) Chen, Y. X.; Chen, S. P.; Zhou, Z. Y.; Tian, N.; Jiang, Y. X.; Sun, S. G.; Ding, Y.; Wang, Z. L. *J. Am. Chem. Soc.* **2009**, *131*, 10860–10862.
(15) Yang, H. G.; Sun, C. H.; Qiao, S. Z.; Zou, J.; Liu, G.; Smith, S. C.; Cheng, H. M.; Lu, G. Q. *Nature* **2008**, *453*, 638–641.
(16) Lai, Z. C.; Peng, F.; Wang, H. J.; Yu, H.; Zhang, S. Q.; Zhao, H. J. *J. Mater. Chem. A* **2013**, *1*, 4182–4185.
(17) Lai, Z. C.; Peng, F.; Wang, Y.; Wang, H. J.; Yu, H.; Liu, P. R.; Zhao, H. J. *J. Mater. Chem. A* **2012**, *22*, 23906–23912.

DOI: 10.1021/cs5014305
ACS Catal. 2015, 5, 1155–1163

(18) Xie, X. W.; Li, Y.; Liu, Z. Q.; Haruta, M.; Shen, W. J. *Nature* **2009**, *458*, 746−749.
(19) Si, R.; Flytzani-Stephanopoulos, M. *Angew. Chem. -Int. Ed.* **2008**, *47*, 2884−2887.
(20) Ta, N.; Liu, J. Y.; Chenna, S.; Crozier, P. A.; Li, Y.; Chen, A. L.; Shen, W. J. *J. Am. Chem. Soc.* **2012**, *134*, 20585−20588.
(21) Gao, Y. X.; Wang, W. D.; Chang, S. J.; Huang, W. X. *ChemCatChem.* **2013**, *5*, 3610−3620.
(22) Wang, M.; Wang, F.; Ma, J. P.; Li, M. R.; Zhang, Z.; Wang, Y. H.; Zhang, X. C.; Xu, J. *Chem. Commun.* **2014**, *50*, 292−294.
(23) Niu, Z. Q.; Li, Y. D. *Chem. Mater.* **2014**, *26*, 72−83.
(24) Qiao, Z. A.; Wu, Z. L.; Dai, S. *ChemSusChem* **2013**, *6*, 1821−1833.
(25) Aneggi, E.; Wiater, D.; de Leitenburg, C.; Llorca, J.; Trovarelli, A. *ACS Catal.* **2014**, *4*, 172−181.
(26) Zhou, C. H. C.; Beltramini, J. N.; Fan, Y. X.; Lu, G. Q. M. *Chem. Soc. Rev.* **2008**, *37*, 527−549.
(27) Claus, P.; Brandner, A.; Lehnert, K.; Bienholz, A.; Lucas, M. *Top. Catal.* **2009**, *52*, 278−287.
(28) Yu, H.; Li, J. C.; Yang, G. X.; Peng, F.; Xie, D. L.; Wang, H. J.; Yang, J. *Energy Fuel* **2011**, *25*, 2643−2650.
(29) Yu, H.; Yang, G. X.; Peng, F.; Wang, H. J.; Yang, J. A.; Xie, D. L. *Renew. Energy* **2011**, *36*, 2120−2127.
(30) Zhou, G.; Barrio, L.; Agnoli, S.; Senanayake, S. D.; Evans, J.; Kubacka, A.; Estrella, M.; Hanson, J. C.; Martinez-Arias, A.; Fernandez-Garcia, M.; Rodriguez, J. A. *Angew. Chem. -Int. Ed.* **2010**, *49*, 9680−9684.
(31) Seo, J. G.; Youn, M. H.; Song, I. K. *Int. J. Hydrogen Energy* **2009**, *34*, 1809−1817.
(32) Zhang, C.; Yue, H.; Huang, Z.; Li, S.; Wu, G.; Ma, X.; Gong, J. *ACS Sustainable Chem. Eng.* **2013**, *1*, 161−173.
(33) Wu, G.; Li, S.; Zhang, C.; Wang, T.; Gong, J. *Appl. Catal. B: Environ.* **2014**, *144*, 277−285.
(34) Chen, H. Q.; Yu, H.; Peng, F.; Yang, G. X.; Wang, H. J.; Yang, J.; Tang, Y. *Chem. Eng. J.* **2010**, *160*, 333−339.
(35) Yang, G. X.; Yu, H.; Huang, X. Y.; Peng, F.; Wang, H. J. *Appl. Catal. B: Environ.* **2012**, *127*, 89−98.
(36) Chen, H. Q.; Yu, H.; Peng, F.; Wang, H. J.; Yang, J.; Pan, M. Q. *J. Catal.* **2010**, *269*, 281−290.
(37) Li, G. G.; Li, C. X.; Xu, Z. H.; Cheng, Z. Y.; Lin, J. *CrystEngComm* **2010**, *12*, 4208−4216.
(38) Tang, B.; Ge, J. C.; Zhuo, L. H. *Nanotechnology* **2004**, *15*, 1749−1751.
(39) Hou, B.; Xu, Y.; Wu, D.; Sun, Y. H. *J. Mater. Sci.* **2007**, *42*, 1397−1400.
(40) Levan, T.; Che, M.; Tatibouet, J. M.; Kermarec, M. *J. Catal.* **1993**, *142*, 18−26.
(41) Fatsikostas, A. N.; Kondarides, D. I.; Verykios, X. E. *Catal. Today* **2002**, *75*, 145−155.
(42) Liu, Z. Q.; Zheng, D. Z.; Su, Y. Z.; Liu, Z. L.; Tong, Y. X. *Electrochem. Solid State Lett.* **2010**, *13*, E15−E18.
(43) Ratnasamy, C.; Wagner, J. P. *Catal. Rev.* **2009**, *51*, 325−440.
(44) Lin, Y. C. *Int. J. Hydrog. Energy* **2013**, *38*, 2678−2700.
(45) Wang, F.; Shi, R. J.; Liu, Z. Q.; Shang, P. J.; Pang, X.; Shen, S.; Feng, Z. C.; Li, C.; Shen, W. J. *ACS Catal.* **2013**, *3*, 890−894.
(46) Wang, F.; Ta, N.; Li, Y.; Shen, W. *Chin. J. Catal.* **2014**, *35*, 437−443.
(47) Manoilova, O. V.; Podkolzin, S. G.; Tope, B.; Lercher, J.; Stangland, E. E.; Goupil, J. M.; Weckhuysen, B. M. *J. Phys. Chem. B* **2004**, *108*, 15770−15781.
(48) Wertheim, G. K.; Guggenheim, H. J. *Phys. Rev. B* **1980**, *22*, 4680−4683.
(49) Gallego, G. S.; Mondragon, F.; Tatibouet, J. M.; Barrault, J.; Batiot-Dupeyrat, C. *Catal. Today* **2008**, *133*, 200−209.
(50) Olafsen, A.; Fjellvag, H. *J. Mater. Chem.* **1999**, *9*, 2697−2702.

DOI: 10.1021/cs5014305
ACS Catal. 2015, 5, 1155−1163